Dispersion control with a Fourier-domain optical delay line in a fiber-optic imaging interferometer

Kye-Sung Lee, A. Ceyhun Akcay, Tony Delemos, Eric Clarkson, and Jannick P. Rolland

Recently, Fourier-domain (FD) optical delay lines (ODLs) were introduced for high-speed scanning and dispersion compensation in imaging interferometry. We investigate the effect of first- and second-order dispersion on the photocurrent signal associated with an optical coherence imaging system implemented with a single-mode fiber, a superluminescent diode centered at 950 nm ± 35 nm, a FD ODL, a mirror, and a layered $LiTAO_3$ that has suitable dispersion characteristics to model a skin specimen. We present a practical and useful method to minimize the effect of dispersion through the interferometer and the specimen combined, as well as to quantify the results using two general metrics for resolution. Theoretical and associated experimental results show that, under the optimum solution, the maximum broadening of the point-spread function through a 1-mm-deep specimen is limited to 57% of its original rms width value (i.e., 8.1 μm optimal, 12.7 μm at maximum broadening) compared with approximately 110% when compensation is performed without the specimen taken into account.

OCIS codes: 120.3180, 170.4500, 170.0110.

1. Introduction

Fiber-optic imaging interferometers such as those employed in optical coherence tomography (OCT) have been developed to image backscattered photons from internal structures in biological tissues and other turbid materials accurately, rapidly, and noninvasively by use of the partial temporal coherence of a broadband light source.[1–3] Because of the broadband nature of the light source, dispersion is an important issue in imaging interferometry because the fiber optics, the specimen, and other dispersive components may have significant dispersion in a fiber-optic interferometer. A dispersion mismatch between the interferometer arms affects the temporal width and shape of the interferometric signal formed by the low-coherence interferometer and consequently affects the longitudinal resolution of the imaging system. Therefore balancing dispersion between the reference and the specimen arms in low-coherence interferometry is necessary to achieve the highest possible axial resolution throughout the imaging depth of the specimen.

There are two approaches to compensate dispersion. One is a postimaging digital technique such as numerical dispersion compensation; the other is a preimaging optical technique. Within postimaging compensation, numerical algorithms based on the fast Fourier transform[4] or the numerical correlation of the depth scan signal with a depth variant kernel[5] were presented to computationally correct the effect of material dispersion on OCT signal data. An autofocus algorithm was also presented for rapid image correction.[6] Recently, other numerical methods based on Fourier-transform techniques were adopted to compensate dispersion in spectral domain OCT by correcting the frequency-dependent nonlinear phase of the received spectral OCT signal.[7–9] Within preimaging compensation, optical dispersion balancing between the specimen and the reference arms is typically achieved by placing a dispersive optical element, such as a pair of prisms employed as a variable thickness dispersive plate, in the reference arm. More recently, a Fourier-domain (FD) optical delay line (ODL) was presented for dispersion compensation,[10] an approach that is the focus of this paper. The FD ODL was first introduced for high-speed scanning[11,12] and proposed for the potential assessment of dispersion in the sample.[13] In addition to these methods, numerical and optical methods were also used together,[14] and the methods used either the frequency entanglement of a twin-photon source[15] or

K.-S. Lee, A. C. Akcay, T. Delemos, and J. P. Rolland (jannick@odalab.ucf.edu) are with the College of Optics and Photonics, Center for Research and Education in Optics and Lasers, Florida Photonics Center of Excellence, University of Central Florida, Orlando, Florida 32816. E. Clarkson is with the Department of Radiology, University of Arizona, Tucson, Arizona 85720.

Received 11 May 2004; revised manuscript received 29 October 2004; accepted 2 December 2004.

0003-6935/05/194009-14$15.00/0

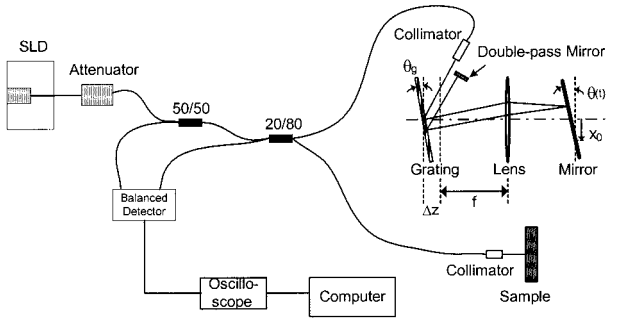

Fig. 1. Schematic diagram of a fiber-optic imaging interferometer with a frequency-domain ODL in the reference arm.

proposed an optimal center wavelength for the source where the dispersion of water in tissue was ineffective.[16]

The schematic diagram of a FD ODL is shown in the reference arm of the fiber-optic interferometer in Fig. 1. A collimated beam is incident on a diffraction grating and dispersed spatially. After propagating through the lens, the light is then projected on a tiltable mirror. The pivot point of the mirror can be offset from the optical axis by a distance x_0. The reflected, dispersed light is focused back onto the grating through the lens and then reflected by a double-pass mirror. The double-pass mirror returns the light to the collimator through the same path of the light propagated. The dispersion introduced by the FD ODL in the reference arm of the fiber-optic interferometer can be controlled by the grating axial shift Δz from the focal plane of the lens, as well as the tilt angle θ_g of the grating normal with respect to the optical axis of the FD ODL.[17] Therefore the grating axial shift and tilt angle have an effect on the axial point-spread function (PSF), which is the envelope of the interferometric autocorrelation of the optical field reflected from the specimen and the optical field reflected from the reference mirror of the FD ODL. Consequently, these parameters do effect the axial resolution.

In this paper the novelty of our research lies in the derivation of the photocurrent signal function in the interferometer accounting for up to second-order dispersion, together with an experimental validation of the theoretical predictions. Furthermore, we propose a practical and useful optical method using a FD ODL to minimize the broadening effect of first-order dispersion and asymmetry of second-order dispersion on the PSF throughout a layered material. The method is experimentally demonstrated for a layered $LiTAO_3$ material having a similar dispersion at 950 nm as a skin specimen.

In Section 2 the theoretical framework derived to perform the simulations is presented. In Subsection 2.A we present an expression or the photocurrent signal in the interferometer, and in Subsection 2.B we provide the relation between the first-order dispersion effects of the FD ODL and that induced by the fiber-length mismatch between the two interferometer arms. Simulations and experimental validations are presented in Section 3. In Subsection 3.A we present the photocurrent signal with up to second-order dispersion. Also, the effect of first- and second-order dispersion caused by the fiber-length mismatch between the two arms is quantified to assess its effect on the photocurrent signal. In Subsection 3.B we consider $LiTAO_3$ in place of the mirror to study the effect of dispersion on the photocurrent given that $LiTAO_3$ has suitable dispersion characteristics to model a skin specimen. The photocurrent signals are investigated both theoretically and experimentally for different dispersion compensation schemes. We then compute the axial resolutions for each case with two resolution metrics that are best suited for asymmetric signal functions. The computed axial resolutions are then compared with each other, and we present an optimum solution for the FD ODL setting, where optimal is defined as the overall highest resolution throughout the imaging depth of the specimen.

2. Theory

In Subsection 2.A we derive the mathematical model of the photocurrent signal at the output of a fiber-optic imaging interferometer employing a FD ODL in one arm and a specimen in the other as shown in Fig. 1. In Subsection 2.B, the quantitative relation between the first-order dispersion effects of the FD ODL and the optical fiber is derived to estimate the optical fiber-length mismatch.

A. Expression of the Photocurrent Signal in a Fiber-Optic Imaging Interferometer with a Fourier-Domain Optical Delay Line

To represent the output signal of the system, we must first start with the input signal, which is the electric field emitted by the source. Given the broadband nature of the light source, it is desirable to express this field by its Fourier components as

$$\mathbf{E}_s(t) = \int_{-\infty}^{\infty} \exp(i\omega t)\hat{E}_s(\omega)\mathrm{d}\omega, \tag{1}$$

where the caret (ˆ) denotes a function in the Fourier domain. Bold letters denote vectors or matrices. Next we can express the field at the detector in terms of the field at the source as

$$\mathbf{E}(t) = \int_{-\infty}^{\infty} \alpha_1 \exp[i\phi_1(\omega, t) + i\omega t]\hat{\mathbf{E}}_s(\omega)\mathrm{d}\omega + \int_{-\infty}^{\infty} \hat{\alpha}_2(\omega)\exp[i\phi_2(\omega, t) + i\omega t]\hat{\mathbf{E}}_s(\omega)\mathrm{d}\omega, \tag{2}$$

where the first term is the electric field from the reference arm and the second term is the electric field from the specimen. Because we use vector field theory, the expression given in Eq. (2) applies to any

state of polarization. The term $\alpha_1 \exp[i\phi_1(\omega, t) + i\omega t]$ contains a real number α_1 that is the relative amplitude at the detector of the wave reflected from the mirror in the FD ODL and the phase $\phi_1(\omega, t)$ that accounts for the optical path length to the mirror and the associated phase change along the path. We can use the FD ODL in the reference arm to induce a phase change, which is a function of frequency. The function $\hat{\alpha}_2(\omega)$ is the amplitude at the detector of the component of the wave backscattered from the specimen at the frequency ω and is determined by the refractive-index profile of the specimen. Finally, the term $\phi_2(\omega, t)$ accounts for the optical path length in the specimen arm and the associated phase changes caused, for example, by reflection, dispersion, and movement of the specimen among other possible effects. If we write

$$m(\omega, t) = \alpha_1 \exp[i\phi_1(\omega, t)] + \hat{\alpha}_2(\omega)\exp[i\phi_2(\omega, t)], \quad (3)$$

then we have

$$\mathbf{E}(t) = \int_{-\infty}^{\infty} m(\omega, t)\exp(i\omega t)\hat{\mathbf{E}}_s(\omega)\mathrm{d}\omega. \quad (4)$$

In Eq. (4) both $\mathbf{E}(t)$ and $\hat{\mathbf{E}}_s(\omega)$ are stochastic processes. Because of its broadband nature we assume that the source field $\mathbf{E}_s(t)$ obeys circular Gaussian statistics.[18] This assumption implies that $\mathbf{E}(t)$ is also a Gaussian random process. In particular, the mean source field satisfies

$$\langle \mathbf{E}_s(t) \rangle = 0,$$

which implies that

$$\langle \mathbf{E}(t) \rangle = 0.$$

Given that the detector has an integration time of Δt, the detected photocurrent is given by

$$I(t) = \frac{e}{\Delta t}\int_{-\Delta t}^{t} N(t')\mathrm{d}t' = \frac{e}{\Delta t}\int_{-\infty}^{\infty} r(t - t')N(t')\mathrm{d}t', \quad (5)$$

where e is the electron charge and $r(t)$ denotes the time integration window of the detector, which is given by

$$r(t) = \begin{matrix} 1 \text{ for } 0 \le t \le \Delta t \\ 0 \text{ otherwise} \end{matrix}. \quad (6)$$

In this integral, $N(t)$ is a doubly stochastic Poisson random process representing the photoelectrons produced by the field impinging on the detector. Its mean is then given by

$$\langle\langle N(t) \rangle\rangle = \rho\langle \mathbf{E}^{\dagger}(t)\mathbf{E}(t) \rangle, \quad (7)$$

where ρ is proportional to the detector responsivity and area, and the double angled brackets are used to indicate statistical averages over the two sources of randomness. Therefore the mean current is given by

$$\langle\langle I(t) \rangle\rangle = \frac{e}{\Delta t}\int_{-\infty}^{\infty} r(t - t')\langle\langle N(t') \rangle\rangle \mathrm{d}t'. \quad (8)$$

The expectation in the integrand is given by

$$\langle\langle N(t') \rangle\rangle = \rho \int_{-\infty}^{\infty}\int_{-\infty}^{\infty} m^*(\omega, t')m(\omega', t') \times \exp[i(\omega' - \omega)t']\langle \hat{\mathbf{E}}_s^{\dagger}(\omega)\hat{\mathbf{E}}_s(\omega') \rangle \mathrm{d}\omega\mathrm{d}\omega'. \quad (9)$$

We assume that the source field is a stationary random process and define the scalar autocovariance function of the source field as

$$G(\tau) = \langle \hat{\mathbf{E}}_s^{\dagger}(t - \tau)\mathbf{E}_s(t) \rangle. \quad (10)$$

The stationarity assumption is related to the stability of the source. This assumption can be relaxed to quasi-stationarity to account for other sources of variation in the source field. The scalar autocovariance function has the property

$$G^*(\tau) = G(-\tau), \quad (11)$$

which ensures that the Fourier transform $\hat{G}(\omega)$ is real. The expectation $\langle \hat{\mathbf{E}}_s^{\dagger}(\omega)\hat{\mathbf{E}}_s(\omega') \rangle$ from Eq. (9) can be expressed by means of the inverse Fourier transform as

$$\begin{aligned} \langle \hat{\mathbf{E}}_s^{\dagger}(\omega)\hat{\mathbf{E}}_s(\omega') \rangle &= \frac{1}{4\pi^2}\int_{-\infty}^{\infty}\int_{-\infty}^{\infty} \exp[-i(\omega' t_2 - \omega t_1)] \\ &\quad \times \langle \mathbf{E}_s^{\dagger}(t_1)\mathbf{E}_s(t_2) \rangle \mathrm{d}t_1\mathrm{d}t_2 \\ &= \frac{1}{4\pi^2}\int_{-\infty}^{\infty}\int_{-\infty}^{\infty} \exp[-i(\omega' t_2 - \omega t_1)] \\ &\quad \times G(t_2 - t_1)\mathrm{d}t_1\mathrm{d}t_2. \end{aligned} \quad (12)$$

By using

$$\omega' t_2 - \omega t_1 = \frac{1}{2}(\omega' - \omega)(t_2 + t_1) + \frac{1}{2}(\omega' + \omega)(t_2 - t_1), \quad (13)$$

we can reduce Eq. (12) to

$$\langle \hat{\mathbf{E}}_s^{\dagger}(\omega)\hat{\mathbf{E}}_s(\omega')\rangle = \frac{1}{2\pi}\,\delta(\omega'-\omega)\int_{-\infty}^{\infty} \times \exp\left[-i\,\frac{(\omega'+\omega)}{2}\,s\right]G(s)\mathrm{d}s = \delta(\omega'-\omega)\hat{G}(\omega). \quad (14)$$

Hereafter $\hat{G}(\omega)$ is represented as $S(\omega)$, which is the power spectral density of the source. Inserting $\langle \hat{\mathbf{E}}_s^{\dagger}(\omega)\hat{\mathbf{E}}_s(\omega')\rangle$ into Eq. (9) yields

$$\langle\langle N(t')\rangle\rangle = \rho\int_{-\infty}^{\infty} |\,m(\omega,t')\,|^2 S(\omega)\mathrm{d}\omega. \quad (15)$$

In the integrand we have

$$|\,m(\omega,t')\,|^2 = \alpha_1{}^2 + |\,\hat{\alpha}_2(\omega)\,|^2 + 2\alpha_1\,\mathrm{Re}\{\hat{\alpha}_2(\omega) \times \exp[-\mathrm{i}\phi_1(\omega,t') + i\phi_2(\omega,t')]\}. \quad (16)$$

The last term is the interference term, which is usually the focus of detection. Combining Eqs. (15) and (8) further yields

$$\langle\langle I(t)\rangle\rangle = \frac{\rho e}{\Delta t}\int_{-\infty}^{\infty} r(t-t') \times \left[\int_{-\infty}^{\infty} |\,m(\omega,t')\,|^2 S(\omega)\mathrm{d}\omega\right]\mathrm{d}t'. \quad (17)$$

If we assume that the response time of the detector is instantaneous, i.e., $r(t-t') = \delta(t-t')$, Eq. (17) simplifies to

$$\langle\langle I(t)\rangle\rangle = \frac{\rho e}{\Delta t}\int_{-\infty}^{\infty} |\,m(\omega,t)\,|^2 S(\omega)\mathrm{d}\omega. \quad (18)$$

To first quantify the effect of dispersion from the fiber and the FD ODL, the specimen is taken to be a mirror. We then introduce the effect of the biological specimen. With the mirror as the specimen, $\hat{\alpha}_2(\omega)$ can be replaced by α_2, and Eq. (16) can be written as

$$|\,m(\omega,t)\,|^2 = \alpha_1{}^2 + \alpha_2{}^2 + 2\alpha_1\alpha_2\,\mathrm{Re}\{\exp[-i\phi_1(\omega,t) + i\phi_2(\omega,t)]\}. \quad (19)$$

When we filter out the dc term of the photocurrent signal, the remaining ac term representing the interference can be written as

$$\langle\langle I_{\mathrm{ac}}(t)\rangle\rangle \propto \int_{-\infty}^{\infty} \mathrm{Re}\{\exp i[\phi_2(\omega,t)-\phi_1(\omega,t)]\}S(\omega)\mathrm{d}\omega \propto \int_{-\infty}^{\infty} \mathrm{Re}[\exp i\Delta\phi(\omega,t)]S(\omega)\mathrm{d}\omega. \quad (20)$$

The phase difference $\Delta\phi(\omega,t)$ can be expanded as a Taylor series as follows:

$$\Delta\phi(\omega,t) = \phi_2(\omega,t) - \phi_1(\omega,t) = \omega_0 t_p(t) + (\omega-\omega_0)t_g(t) + D_\omega(t)\,\frac{(\omega-\omega_0)^2}{2!} + D_\omega^{(1)}(t)\,\frac{(\omega-\omega_0)^3}{3!} + \cdots, \quad (21)$$

ω_0 is the center frequency of the light source, $t_p(t)$ is the phase delay, $t_g(t)$ is the group delay, $D_\omega(t)$ is the first-order group-delay dispersion, and $D_\omega^{(1)}(t)$ is the second-order group-delay dispersion. Furthermore each parameter can be further defined as

$$t_p(t) \equiv \Delta\phi(\omega_0,t)/\omega_0,$$

$$t_g(t) \equiv \partial[\Delta\phi(\omega,t)]/\partial\omega\,|_{\omega=\omega_0},$$

$$D_\omega(t) \equiv \partial^2[\Delta\phi(\omega,t)]/\partial\omega^2\,|_{\omega=\omega_0},$$

$$D_\omega^{(1)}(t) \equiv \partial^3[\Delta\phi(\omega,t)]/\partial\omega^3\,|_{\omega=\omega_0}. \quad (22)$$

Inserting Eq. (21) up to the fourth terms into relation (20), $\langle\langle I_{\mathrm{ac}}(t)\rangle\rangle$ can be expressed as

$$\langle\langle I_{\mathrm{ac}}(t)\rangle\rangle \propto \mathrm{Re}\left(\int_{-\infty}^{\infty} S(\omega-\omega_0)\exp\left\{i\left[D_\omega\,\frac{(\omega-\omega_0)^2}{2!} + D_\omega^{(1)}\,\frac{(\omega-\omega_0)^3}{3!}\right]\right\}\right)\exp(i\omega_0 t_p)\exp[i(\omega-\omega_0)t_g]\mathrm{d}\omega, \quad (23)$$

where $S(\omega-\omega_0)$ is the source power spectral density centered at ω_0. It can be observed that relation (23) is the inverse Fourier transform of the frequency-domain function given by

$$\hat{\mathbf{I}}_{\mathrm{ac}}(\omega') \propto S(\omega')\exp\left\{i\left[D_\omega\,\frac{\omega'^2}{2!} + D_\omega^{(1)}\frac{\omega'^3}{3!}\right]\right\}\exp(i\omega_0 t_p), \quad (24)$$

where $\omega' = \omega - \omega_0$. We now apply relation (24) to the fiber-optic interferometer with a FD ODL in the reference arm. However, we first need to establish some expressions for the phase and group delays, as well as the first- and second-order group-delay dispersion associated with the FD ODL. Zvyagin *et al.*[17] derived expressions for $t_{p\,\mathrm{ODL}}(t)$, $t_{g\,\mathrm{ODL}}(t)$, $D_{\omega\,\mathrm{ODL}}(t)$, and $D_{\omega\,\mathrm{ODL}}^{(1)}(t)$ in a FD ODL, which have been adapted here for a double-pass system. Such expressions are derived in Appendix A and given by

$$t_{p\ \mathrm{ODL}}(t) = \frac{4\Delta z}{c} + \frac{4\Delta\theta(t)x_0}{c}, \tag{25}$$

$$t_{g\ \mathrm{ODL}}(t) = \frac{4\Delta z}{c} + \frac{4\Delta\theta(t)x_0}{c} + \frac{8\pi\Delta\theta(t)f}{p\omega_0 \cos\theta_g}, \tag{26}$$

$$D_{\omega,\ \mathrm{ODL}}(t) = -\frac{16\pi^2 c[\Delta z + f\Delta\theta(t)\tan\theta_g]}{p^2{\omega_0}^3 \cos^2\theta_g}, \tag{27}$$

$$D^{(1)}_{\omega,\ \mathrm{ODL}}(t) = \frac{48\pi^2 c[\Delta z + f\Delta\theta(t)\tan\theta_g]}{p^2{\omega_0}^4 \cos^2\theta_g} \times \left(1 + \frac{2\pi c \sin\theta_g}{p\omega_0 \cos^2\theta_g}\right), \tag{28}$$

where p is the grating period, f is the focal length of the lens, Δz is the axial shift of the grating with respect to the focal plane of the lens, θ_g is the tilt of the grating with respect to the lens, x_0 is the lateral offset of the pivot point of the scanning mirror with respect to the optical axis of the lens, $\Delta\theta(t)$ is the scan angle of the mirror, and c is the speed of light.

With the set of Eqs. (25)–(28), the effect of both the fiber-length mismatch between two arms and the effect of the specimen can be added to the equations of a double-pass FD ODL as follows:

$$t_p(t) = t_{p\ \mathrm{ODL}}(t) + t_{p\ \mathrm{fiber}}(t) + t_{p\ \mathrm{sample}}(t) = \frac{4\Delta z}{c} + \frac{4\Delta\theta(t)x_0}{c} + \frac{2\delta}{c} - \frac{2\Delta d_s}{\nu_{p\ \mathrm{sample}}}, \tag{29}$$

$$t_g(t) = t_{g\ \mathrm{ODL}}(t) + t_{g\ \mathrm{fiber}}(t) + t_{g\ \mathrm{sample}}(t) = \frac{4\Delta z}{c} + \frac{4\Delta\theta(t)x_0}{c} + \frac{8\pi\theta(t)f}{p\omega_0 \cos\theta_g} + \frac{2\delta}{c} - \frac{2\Delta d_s}{\nu_{g\ \mathrm{sample}}}, \tag{30}$$

where δ is the potential optical path-length mismatch $l_r - l_s$ between the reference arm and the specimen arm, l_r is the optical path length in the reference arm, l_s is the optical path length in the specimen arm up to the specimen surface, and Δd_s is the depth of penetration in the specimen. The mismatch is caused by the implementation challenge in setting an equal fiber length in both arms of the interferometer. The phase velocity $\nu_{p\ \mathrm{sample}}$ is given by $c/n_{p\ \mathrm{sample}}$, and the group velocity $\nu_{g\ \mathrm{sample}}$ is given by $c/n_{g\ \mathrm{sample}}$, where $n_{p\ \mathrm{sample}}$ is the mean refractive index of the specimen, and the group-velocity index $n_{g\ \mathrm{sample}}$ is given by $n_{p\ \mathrm{sample}} - \lambda(\mathrm{d}n_{p\ \mathrm{sample}}/\mathrm{d}\lambda)$. The overall first- and second-order dispersion equations in the interferometer caused by the FD ODL, the fiber-length mismatch, and the specimen are given by

$$D_\omega(t) = D_{\omega\ \mathrm{ODL}}(t) + D_{\omega\ \mathrm{fiber}}(t) + D_{\omega\ \mathrm{sample}}(t) = -\frac{16\pi^2 c[\Delta z + f\Delta\theta(t)\tan\theta_g]}{p^2{\omega_0}^3 \cos^2\theta_g} + 2\beta_{2\ \mathrm{fiber}}\Delta d - 2\beta_{2\ \mathrm{sample}}\Delta d_s, \tag{31}$$

$$D^{(1)}_\omega(t) = D^{(1)}_{\omega\ \mathrm{ODL}}(t) + D^{(1)}_{w\ \mathrm{fiber}}(t) + D^{(1)}_{w\ \mathrm{sample}}(t) = \frac{48\pi^2 c[\Delta z + f\Delta\theta(t)\tan\theta_g]}{p^2{\omega_0}^4 \cos^2\theta_g}\left(1 + \frac{2\pi c \sin\theta_g}{p\omega_0 \cos^2\theta_g}\right) + 2\beta_{3\ \mathrm{fiber}}\Delta d - 2\beta_{3\ \mathrm{sample}}\Delta d_s, \tag{32}$$

where Δd is the fiber-length mismatch $d_r - d_s$ between the reference arm and the specimen arm; d_r is the fiber length in the reference arm; d_s is the fiber length in the specimen arm; $\beta_{2\ \mathrm{fiber}}$ and $\beta_{2\ \mathrm{sample}}$ are the first-order dispersion coefficient of the fiber and the specimen, respectively; and similarly $\beta_{3\ \mathrm{fiber}}$ and $\beta_{3\ \mathrm{sample}}$ are the second-order dispersion coefficient of the fiber and the specimen, respectively. In Eqs. (31) and (32) we define the dispersion in the reference arm to be positive if the reference arm fiber is longer than the specimen arm fiber (i.e., $\Delta d > 0$). Therefore the dispersion in the specimen arm, which can be introduced by a specimen, should be negative because $D_\omega(t)$ or $D^{(1)}_\omega$ would be zero if the first-order or second-order dispersion in both arms were the same, i.e., they cancel each other. The FD ODL is employed to induce negative or positive dispersion in the reference arm depending on Δd and the dispersion characteristics of the specimen to match the total first- or second-order dispersion in the interferometer arms.

B. Relation Between the First-Order Dispersion Effects of the Fourier-Domain Optical Delay Line and the Optical Fiber

With a mirror employed as the specimen, the relation between the first-order dispersion owing to fiber-length mismatch Δd and the first-order dispersion owing to the axial grating shift Δz of the FD ODL with respect to the focal plane of the lens can be investigated. An axial shift of the tiltable mirror of the FD ODL with respect to the lens will not affect dispersion because the lens is telecentric in the space of the mirror. This axial shift would simply add a constant optical path length to all wavelengths and also decrease the coupling efficiency in the interferometer. To determine the amount of axial shift of the grating that induces a first-order dispersion equal to the first-order dispersion imposed by a given fiber-length mismatch in the interferometer arms, we derive a relation from Eq. (31) given by

$$D_\omega(t) = D_{\omega\ \mathrm{ODL}}(t) + D_{\omega\ \mathrm{fiber}}(t) = -\frac{16\pi^2 c[\Delta z + f\Delta\theta(t)\tan\theta_g]}{p^2{\omega_0}^3 \cos^2\theta_g} + 2\beta_{2\ \mathrm{fiber}}\Delta d. \tag{33}$$

The first-order dispersion is related to Δz as well as to the tilt angle of the mirror $\Delta\theta(t)$, which can be a sinusoidal or a triangular function of time in the case where θ_g is nonzero. Therefore the dispersion would be a time-varying function if the grating tilt angle was nonzero. Compensation of a time-varying dispersion would need a dynamic grating axial shift synchronized to the tilt angle of the mirror, which is

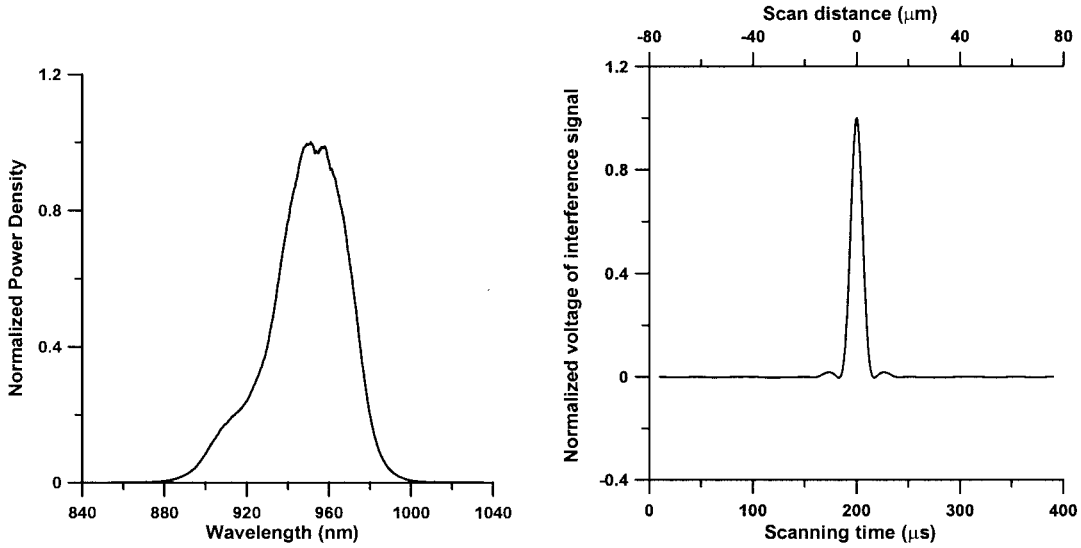

(a) (b)

Fig. 2. (a) Measured power spectral density of the SLD, (b) corresponding ideal photocurrent signal.

complicated to accomplish. Hence we set the tilt of the grating θ_g to zero. Therefore the relation between the amount of axial shift Δz of the grating from the focal plane of a lens and a fiber-length mismatch Δd to make the overall first-order dispersion $D_\omega(t)$ zero is given by

$$\frac{\Delta z}{\Delta d} = \frac{\beta_{2\,\mathrm{fiber}} p^2 {\omega_0}^3}{8\pi^2 c}. \tag{34}$$

Thus the axial shift Δz required to remove the first-order dispersion caused by the fiber-length mismatch Δd can be set according to the first-order dispersion coefficient of the fiber $\beta_{2\,\mathrm{fiber}}$, the grating period p, and the center frequency of the source ω_0, all known or measurable parameters. Therefore the ratio provided by Eq. (34) can be computed, and if either one of the two parameters Δz or Δd was known, the other could then be determined. In practice, Δz can be theoretically established and Δd can then be computed by use of Eq. (34) as detailed in Subsection 3.A.

3. Simulation and Experimental Validation

In a dispersionless system the power spectral density of the superluminescent diode (SLD) and its autocorrelation function form a Fourier-transform pair as given by the Wiener–Khinchin theorem.[19] Figure 2(a) shows the measured power spectral density of the SLD, and Fig. 2(b) presents the corresponding photocurrent signal simulated by taking the inverse Fourier transform of the measured power spectral density of the SLD. Given the power spectral density of the SLD shown in Fig. 2(a), Fig. 2(b) presents the ideal photocurrent signal.

We implemented the fiber-optic interferometer shown in Fig. 1. A SLD (SLD-47HP Superlum Diodes) centered at 950 nm with a spectral bandwidth of approximately 70 nm and a power of 7 mW illuminated the interferometer. An attenuator was employed to prevent optical feedback into the SLD, which would cause permanent damage to the source. A circulator or isolator centered at 950 nm and of large bandwidth would have been preferred but such components are not yet commercially available. The light emitted by the SLD went through two fused fiber couplers. A splitting ratio of 80/20 enabled transmission of maximum power into the specimen, reducing the excess noise arising from the reference arm. Figure 1 also shows the FD ODL that was used for depth scanning and dispersion compensation. We used a balanced detector (Nirvana 2017) connected to a real-time oscilloscope (Tektronix TDS210) to observe the photocurrent signal. The oscilloscope was connected to a computer that was employed to record the signal.

In Subsection 3.A we combine experimental research with the theoretical analysis of dispersion in the interferometer up to second order given in Section 2. We first employ a mirror as the specimen and then analyze the effect of first- and second-order dispersion effects on the photocurrent signal. We then perform first-order dispersion compensation by adjusting Δz in the FD ODL to improve the degraded photocurrent signal. In Subsection 3.B we simulate and demonstrate experimentally the effect of dispersion with a $LiTaO_3$ specimen that was chosen because of its suitable dispersion characteristics to model a skin specimen.

A. First-Order Dispersion Compensation and Effect of Second-Order Dispersion on the Photocurrent Signal when the Specimen is a Mirror

The parameters related to the single-mode optical fiber and the FD ODL are given in Table 1. Inserting

Table 1. Parameters of the Single-Mode Optical Fiber and the FD ODL

λ_0	$\beta_{2\,\mathrm{fiber}}$ at λ_0	$\beta_{3\,\mathrm{fiber}}$ at λ_0	p	f	$\Delta\theta_{\max}(t)$
950 nm	34.95 fs^2/mm	420 fs^3/mm	1.204 μm	25 mm	2°

these parameters into Eq. (34), we obtained the ratio $\Delta z/\Delta d = 0.0168$.

The grating was set to be parallel to the lens so that the tilt angle of the grating was zero. To obtain the narrowest photocurrent signal, we shifted the grating axially to match the first-order dispersion in the arms of the fiber-optic interferometer. We then simulated the photocurrent signal of the system by theoretically varying Δz and x_0. The value of x_0, validated theoretically, was set experimentally at 0.4 mm. Such a value enforces a low modulation frequency of the photocurrent signal, which is directly proportional to x_0 as shown in Eqs. (24) and (25). Δz was set at 0.06 mm and validated theoretically as well. The fiber-length mismatchΔd was then computed to be 3.6 mm by use of Eq. (34). Figure 3(a) shows the narrowest photocurrent signal obtained experimentally by adjusting the grating axial shift Δz to compensate the first-order dispersion induced by the fiber-length mismatch. Figure 3(b) represents the corresponding photocurrent signal simulated with $\Delta z = 0.06$ mm, $\Delta d = 3.6$ mm, and $x_0 = 0.4$ mm. Figures 3(a) and 3(b) show that the first-order dispersion induced by $\Delta z = 0.06$ mm compensates the first-order dispersion induced by the 3.6 mm of fiber-length mismatch between the two arms. Under such a setting, there remains no overall first-order dispersion. However, the second-order dispersion corresponding to $\Delta z = 0.06$ mm and $\Delta d = 3.6$ mm is nonzero and is best shown by the asymmetric small oscillations in Figs. 3(a) and 3(b).

To further validate the set value of x_0, we increased Δz from 0.06 to 0.13 mm. The first-order dispersion caused by $\Delta z = 0.06$ mm out of the total grating axial shift $\Delta z = 0.13$ mm compensates the 3.6 mm of the fiber-length mismatch between the two arms because the first-order dispersion due to the FD ODL is linear with the grating axial shift Δz as given by Eq. (27). Thus there remains first-order dispersion due to the grating additional axial shift of 0.07 mm, second-order dispersion due to the overall grating axial shift $\Delta z = 0.13$ mm, and second-order dispersion due to the fiber-length mismatch $\Delta d = 3.6$ mm. The corresponding photocurrent signal is shown in Figs. 4(a) and 4(b).

To isolate the contribution of the first-order dispersion, we also simulated the photocurrent signal shown in Fig. 4(c), where the total second-order dispersion was simply set to zero in the simulation. We next simulated the photocurrent signal shown in Fig. 4(d) by setting the total first-order dispersion in the simulation to zero, so that the contribution of the second-order dispersion could be next isolated and visualized. The results of these simulations show that the asymmetric shape and sidelobes in the photocurrent signal are caused by the total second-order dispersion of the interferometer.

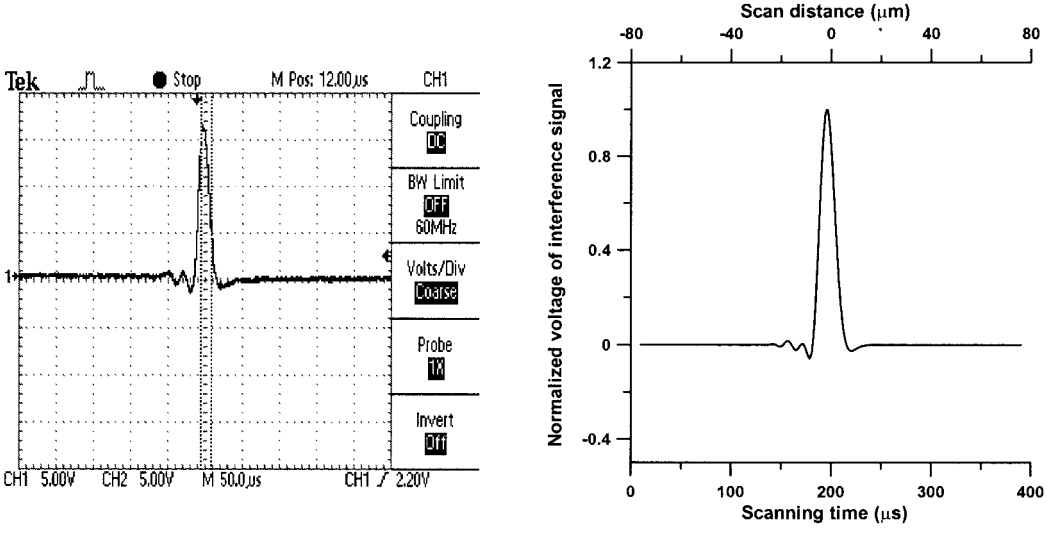

Fig. 3. (a) Experimental result corresponding to the parameters listed in (b); (b) simulation result for $\Delta z = 0.06$ mm, $\Delta d = 3.6$ mm, and $x_0 = 0.4$ mm.

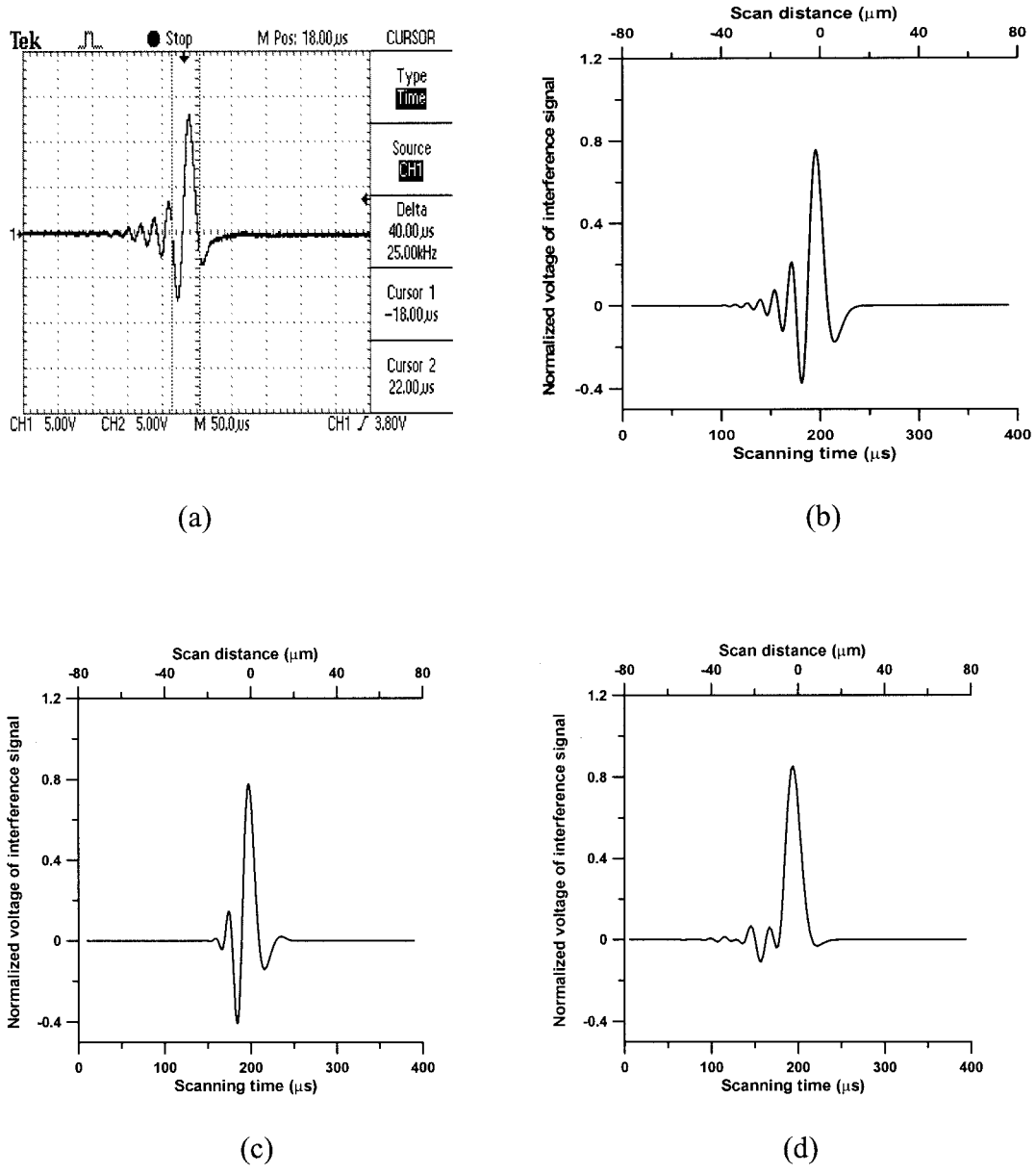

Fig. 4. (a) Experimental result with an additional 0.07-mm axial grating shift from the initial 0.06 mm; (b) simulation result for $\Delta z = 0.13$ mm, $\Delta d = 3.6$ mm, and $x_0 = 0.4$ mm; (c) isolated effect of first-order dispersion; (d) isolated effect of second-order dispersion.

B. Experimental Validation of First-Order Dispersion Compensation and Effect of Second-Order Dispersion on the Photocurrent Signal

In Subsection 3.A we investigated the effect on the signal photocurrent of the first- and second-order dispersion induced by the fiber-length mismatch between the interferometer arms and the FD ODL. We quantified the compensation of the first-order dispersion induced by the fiber-length mismatch using the FD ODL. The specimen employed was a mirror and thus was nondispersive. In this subsection we add the effect of dispersion due to a dispersive specimen on the photocurrent signal. A layered $LiTaO_3$ specimen was selected because of its suitable dispersion characteristics to model a skin specimen. A skin specimen is highly scattering, thus quantifying the effect of dispersion of skin on an isolated photocurrent signal and its envelope is not doable.

Given that the first-order dispersion coefficient of $LiTaO_3$ is approximately twice as large as that of skin at 950 nm as shown in Table 2, a light beam centered at 950 nm obtains the same first-order dispersion after going through 0.5 mm of $LiTaO_3$ as 1.085 mm of

Table 2. Dispersion Coefficients of Skin and $LiTaO_3$

Specimen	β_2 at 950 nm	β_3 at 950 nm
Skin	109 fs^2/mm	159 fs^3/mm
$LiTaO_3$	236.8 fs^2/mm	188 fs^3/mm

skin specimen. The second-order dispersion slight mismatch between the skin and the $LiTaO_3$ specimens is found to be negligible. The dispersion coefficients provided in Table 2 were derived from the formula for the refractive indices of skin and $LiTaO_3$ given as a function of wavelength in Refs. 20 and 21. Using this function and the definitions given in Refs. 22 and 23, we computed the first- and second-order dispersion coefficients β_2 and β_3 of skin and $LiTaO_3$. These coefficients indicate that the first-order dispersion in a skin specimen is large compared with that in the optical fiber, and thus the specimen must be accounted for in any compensation scheme. Since we are focusing in this paper essentially on dispersion and its effect on resolution, we do not model the power loss due to reflections, scattering, and absorption within $LiTaO_3$.

The simulations and experiments of the photocurrent signal were based on the experimental setup described in Subsection 3.A, with the exception that x_0 was increased to 3 mm to modulate the photocurrent signal at a higher frequency where the noise level drops and the signal-to-noise ratio increases. The grating axial shift Δz was set to 0.06 mm, where the first-order dispersion induced by the fiber-length mismatch of 3.6 mm between the interferometer arms was compensated.

The first case presented in Fig. 5 shows the photocurrent signals when the first-order dispersion was compensated for the light reflected from layer *A* indicated with a bold line in Fig. 5(a). The two-dimensional image of the specimen is shown in Fig. 5(b). The photocurrent signals are shown in Fig. 5(c) when two layers of $LiTaO_3$ separated by an air gap of 80 μm were scanned through the single line S shown in Fig. 5(b). Figures 5(d), 5(e), and 5(f) present the zoomed measured photocurrent signal induced by the reflections off layers *A*, *B*, and *C*, respectively. Also shown in Figs. 5(d), 5(e), and 5(f) are the envelopes of the measured photocurrent signal and the envelopes of the simulated photocurrent signal. The broadening and asymmetry of the envelopes of the photocurrent signal caused by uncompensated first- and second-order dispersion induced by $LiTaO_3$ and the FD ODL are observed in Figs. 5(e) and 5(f), and the photocurrent shown in Fig. 5(d) suffers only from second-order dispersion. For the light reflected from the back end of $LiTaO_3$, which is layer *C*, the effect of dispersion is so severe that the corresponding photocurrent signal is broadened maximally.

Observing the severe degradation in the photocurrent signal due to the reflection from the back end of $LiTaO_3$, i.e., from layer *C*, we investigated a case in which the grating of the FD ODL was moved closer to the lens of the FD ODL, i.e., Δz was decreased, so that the total first-order dispersion in the system was zero for the light reflected in the midplane of $LiTaO_3$, i.e., from layer *B*, as shown in Fig. 6(a). We computed the corresponding grating axial shift to be 0.005 mm. Figure 6(c) presents the measured photocurrent signals resulting from reflections off of layers *A*, *B*, and *C*, respectively, through the single line S shown in Fig. 6(b). The zoomed photocurrent signals and their envelopes are shown in Figs. 6(d)–6(f). In this case, the results show a lessened overall broadening of the photocurrent signal envelopes across the depth of the specimen and a weaker effect of first-order dispersion in the photocurrents. The photocurrent signal less affected by the first-order dispersion is naturally the one detected from layer *B* as shown in Fig. 6(e).

To be comprehensive, we investigated a final case, where we further decreased the grating axial shift Δz down to -0.055 mm so that the total first-order dispersion was set to zero for the light reflected at the back end of $LiTaO_3$ shown with a bold line in Fig. 7(a). The severe effect of the first- and second-order dispersion is demonstrated in Fig. 7(d) for the photocurrent signal resulting from the reflection off of layer *A* of the specimen. The photocurrent signal shown in Fig. 7(f) presents a slight effect of second-order dispersion, and Fig. 7(e) shows the photocurrent signal measured from the reflection off of layer *B* of $LiTaO_3$.

Photocurrent signals presented in Figs. 5(d), 6(e), and 7(f) with overall first-order dispersion equal to zero are not the same since the second-order dispersion for each case is different. For example, the photocurrent signal in Fig. 5(d) presents significant sidelobes whereas the one shown in Fig. 7(f) does not possess any significant sidelobes. Therefore we do not necessarily expect the axial resolution for each case to be the same because of the effect of second-order dispersion.

Table 3 presents the computed axial resolutions of the photocurrent signals shown in Figs. 5, 6, and 7 (i.e., l_A, l_B, $l_{B'}$, l_C). The ASI is the absolute square integral of the envelopes of the photocurrent signals and is a metric used to quantify the axial resolution in OCT, and rms width (i.e., σ_{rms}) is the root mean square of the envelopes of the photocurrent signals.[24,25]

With the results presented and Table 3 that quantify resolution, we have shown that the axial resolution in the OCT system is not fixed over the specimen scanned for a biological specimen because of dispersion. When the total first-order dispersion is set to zero for the middle plane of the specimen by shifting the grating of the FD ODL axially, the effect of the first-order dispersion on the photocurrent signal is minimized over the entire depth of the specimen considered for imaging. In the case of this optimal setting, the small broadening and asymmetry combined of the photocurrent signal are a combination of first-order residual dispersion away from the plane of compensation and the associated second-order dispersion, respectively.

4. Conclusion

In this paper we demonstrated the effect of dispersion up to second order in a fiber-optic interferometer that has the general structure of an OCT system. The dispersion effects induced by $LiTaO_3$ were included for its similarity of dispersion characteristics to skin specimens. We presented a theoretical and associated experimental framework for minimizing broadening

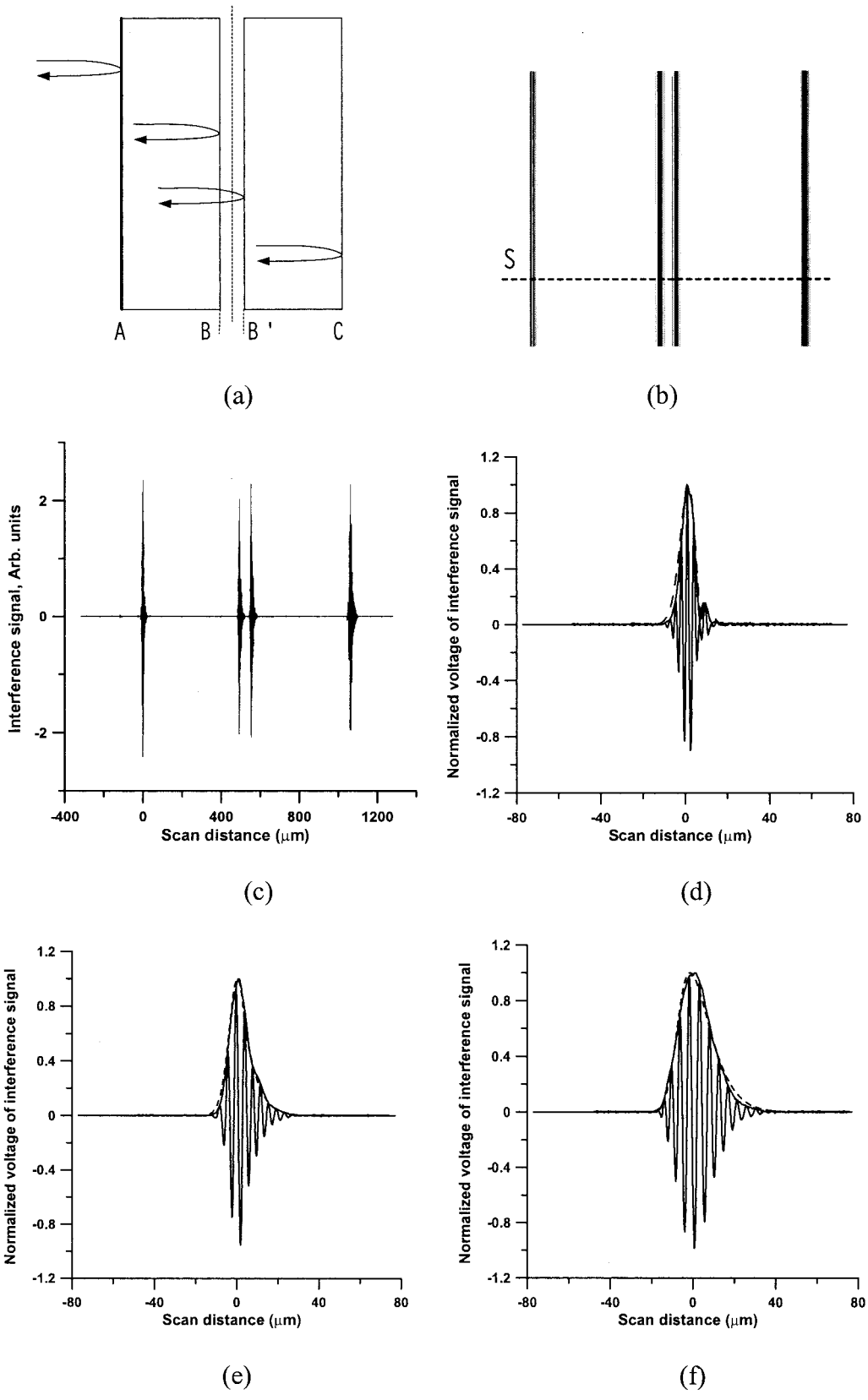

Fig. 5. (a) Schematic of two layers of 0.5-mm $LiTaO_3$ separated by an air gap; (b) two-dimensional image of the specimen when the first-order dispersion compensation is set for the signal reflected off the front surface A of the specimen; (c) single depth scan through the line S shown in (b) of the specimen image; (d)–(f) solid curves are zoomed photocurrent signal envelopes and the dashed curves are simulated photocurrent signal envelopes for light reflected off of (d) the front surface A, (e) the second surface (i.e., from layer B), and (f) the back surface C of the specimen for $\Delta z = 0.06$ mm, $\Delta d = 3.6$ mm, and $x_0 = 3$ mm.

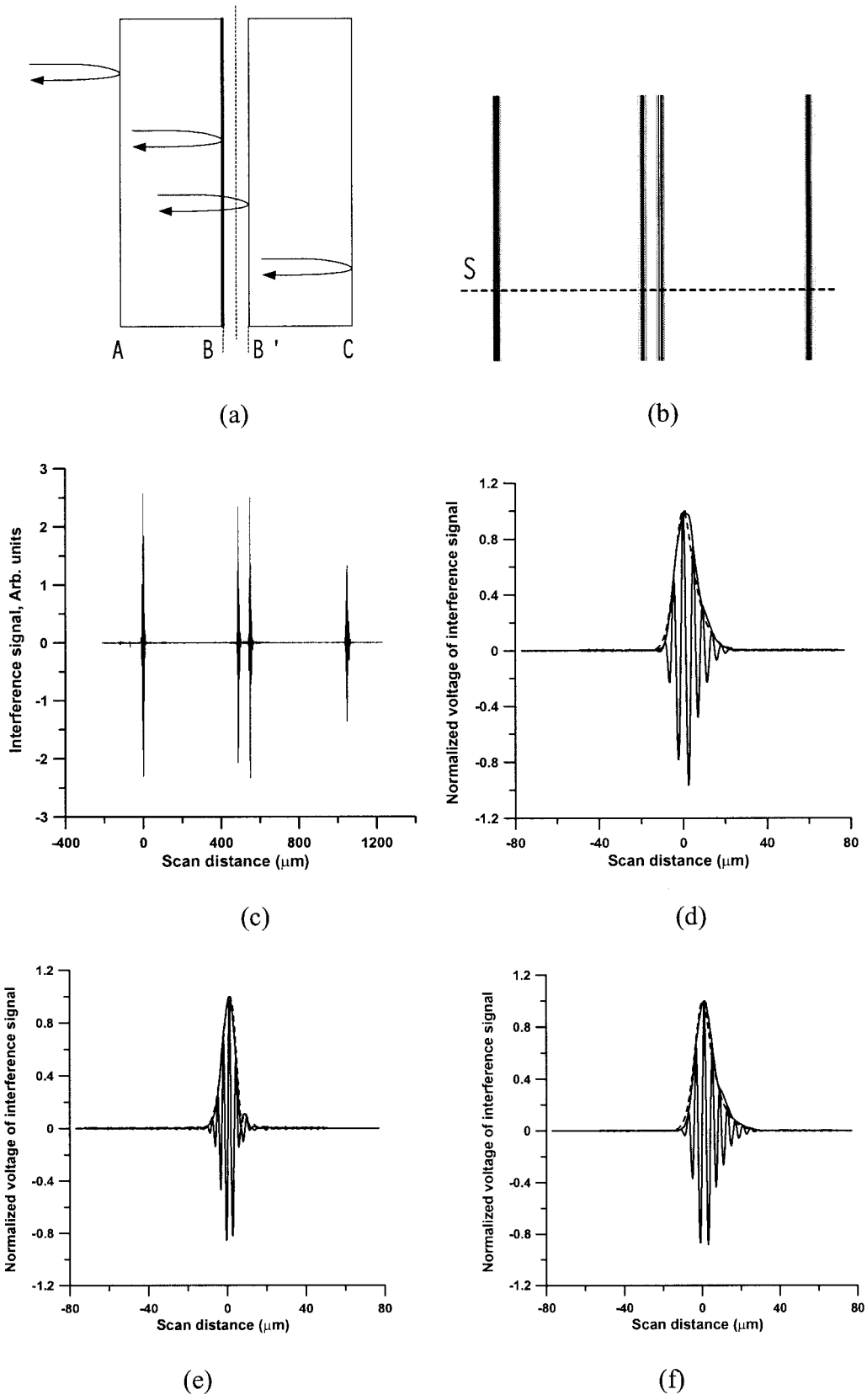

Fig. 6. Schematic of two layers of 0.5-mm $LiTaO_3$ separated by an air gap; (b) two-dimensional image of the specimen when the first-order dispersion compensation is set for the signal reflected off of the middle surface B of the specimen; (c) single depth scan through the line S shown in (b) of the specimen image; (d)–(f) solid curves are zoomed photocurrent signal envelopes and the dashed curves are simulated photocurrent signal envelopes for light reflected off of (d) the front surface A, (e) the second surface (i.e., from layer B), and (f) the back surface C of the specimen for $\Delta z = 0.005$ mm, $\Delta d = 3.6$ mm, and $x_0 = 3$ mm.

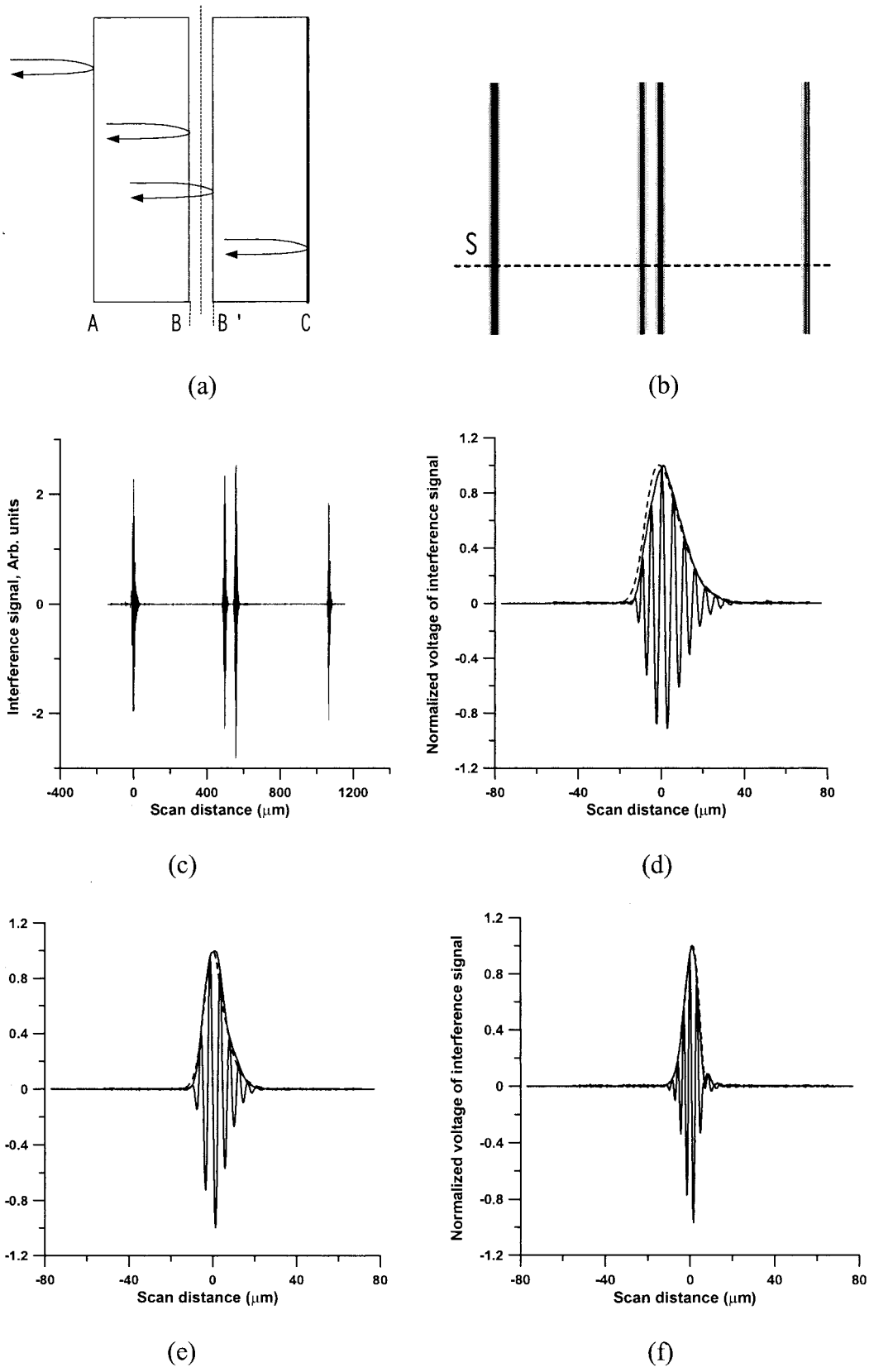

Fig. 7. Schematic of two layers of 0.5-mm $LiTaO_3$ separated by an air gap; (b) two-dimensional image of the specimen when the first-order dispersion compensation is set for the signal reflected off of the back surface C of the specimen; (c) single depth scan through the line S shown in (b) of the specimen image; (d)–(f) solid curves are zoomed photocurrent signal envelopes and the dashed curves are simulated photocurrent signal envelopes for light reflected off (d) the front surface A, (e) the second surface (i.e., from layer B), and (f) the back surface C of the specimen for $\Delta z = -0.055$ mm, $\Delta d = 3.6$ mm, and $x_0 = 3$ mm.

Table 3. Computed Axial Resolutions in $LiTaO_3$

Case	Metric	l_A (μm)	l_B (μm)	$l_{B'}$ (μm)	l_C (μm)
Front surface dispersion compensation	ASI	6.35	8.04	8.04	14.23
	rms width	8.87	12.94	12.94	18.71
Middle surface dispersion compensation	ASI	8.05	6.18	6.18	8.16
	rms width	12.67	8.05	8.05	12.14
Back surface dispersion compensation	ASI	14.45	8.25	8.25	6.00
	rms width	18.34	11.96	11.96	7.33

of the envelopes of the photocurrent signals observed across the depth of the specimen. We quantified how first-order dispersion in the overall system with a biological specimen can be compensated by employing a FD ODL with a grating with variable axial position. Results showed that the second-order dispersion cannot be compensated together with the first-order dispersion. However, we proposed a dispersion compensation method for highest overall axial resolution across the depth of the specimen. Particularly, the method proposed is suitable for imaging a few millimeters deep into the specimen. Specifically, if the overall first-order dispersion compensation is set for the photocurrent signal resulting from the light reflected from around the middle plane of the specimen, the effect of first-order dispersion on the photocurrent signal is overall minimized and resolution is highest across the depth of the specimen.

Appendix A

Zvyagin *et al.*[17] derived the phase difference $\Delta\phi(\omega, t)$ in FD ODL between the phase acquired by a ray of arbitrary frequency ω when $\theta(t)$ is nonzero and the phase acquired when $\theta(t) = 0$, i.e.,

$$\Delta\phi(\omega, t) = \frac{2\omega\Delta z}{c}\cos\beta + \frac{2\omega x_0\theta(t)}{c} - \frac{2\omega\theta(t)f}{c}\sin\beta, \tag{A1}$$

where $\theta(t)$ and β are defined as shown in Fig. 8.

Equation (A1) is changed for a double-pass FD ODL in Fig. 8 as

$$\begin{aligned}\Delta\phi_{\mathrm{ODL}}(\omega, t) &= \frac{4\omega\Delta z}{c}\cos\beta + \frac{4\omega x_0\Delta\theta(t)}{c} \\ &\quad - \frac{4\omega\Delta\theta(t)}{c}\sin\beta \\ &= \frac{4\omega\Delta z}{c} - \frac{8\omega\Delta z}{c}\sin^2\frac{\beta}{2} + \frac{4\omega x_0}{c}\Delta\theta(t) \\ &\quad - \frac{4\omega\Delta\theta(t)f}{c}\sin\beta,\end{aligned} \tag{A2}$$

where $\Delta\theta(t) = \theta(t) - \theta_{\min}$.

The grating equation is used to replace $\sin\beta$ in Eq. (A2), which is given by[17]

$$p[\sin(\beta + \theta_g) - \sin\theta_g] = 2\pi mc\left(\frac{1}{\omega} - \frac{1}{\omega_0}\right). \tag{A3}$$

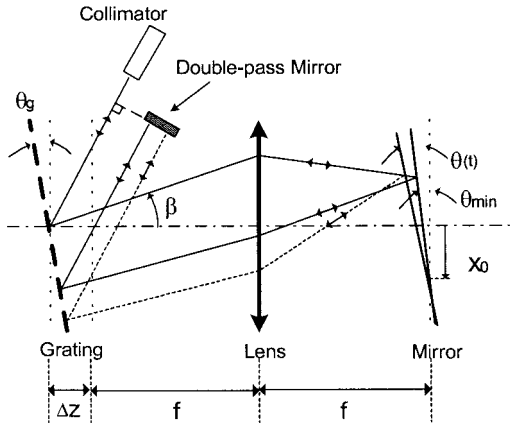

Fig. 8. Schematic diagram of the double-pass FD ODL in the case of a grating tilted from the normal and offset from the focal plane.

The $\Delta\phi_{\mathrm{ODL}}(\omega, t)$ in a double-pass FD ODL is the phase difference between the phase acquired by a ray of arbitrary frequency ω when $\theta(t)$ is nonzero and the phase acquired when $\theta(t)$ is $\theta_{\min}$. We find the phase delay $t_p(t)$, the group delay $t_g(t)$, the first-order group-delay dispersion $D_\omega(t)$, and the second-order group-delay dispersion $D_\omega^{(1)}(t)$ in a double-pass FD ODL by the definitions of each value as

$$t_{p\,\mathrm{ODL}}(t) \equiv \frac{\Delta\phi_{\mathrm{ODL}}(\omega_0, t)}{\omega_0} = \frac{4\Delta z}{c} + \frac{4\Delta\theta(t)x_0}{c}, \tag{A4}$$

$$\begin{aligned}t_{g\,\mathrm{ODL}}(t) &\equiv \left.\frac{\partial[\Delta\phi_{\mathrm{ODL}}(\omega,\ t)]}{\partial\omega}\right|_{\omega=\omega_0} \\ &= \frac{4\Delta z}{c} + \frac{4\Delta\theta(t)x_0}{c} + \frac{8\pi\Delta\theta(t)f}{p\omega_0\cos\theta_g},\end{aligned} \tag{A5}$$

$$\begin{aligned}D_{\omega\mathrm{ODL}}(t) &\equiv \left.\frac{\partial^2[\Delta\phi_{\mathrm{ODL}}(\omega,\ t)]}{\partial\omega^2}\right|_{\omega=\omega_0} \\ &= -\frac{16\pi^2c[\Delta z + f\Delta\theta(t)\tan\theta_g}{p^2{\omega_0}^3\cos^2\theta_g},\end{aligned} \tag{A6}$$

$$\begin{aligned}D_{\omega\,\mathrm{ODL}}^{(1)}(t) &\equiv \left.\frac{\partial^3[\Delta\phi_{\mathrm{ODL}}(\omega,\ t)]}{\partial\omega^3}\right|_{\omega=\omega_0} \\ &= \frac{48\pi^2c[\Delta z + f\Delta\theta(t)\tan\theta_g]}{p^2{\omega_0}^4\cos^2\theta_g}\left(1 + \frac{2\pi c\sin\theta_g}{p\omega_0\cos^2\theta_g}\right).\end{aligned} \tag{A7}$$

We thank Huikai Xie for stimulating discussions about this research. This research was supported in part by the Florida Photonics Center of Excellence, the National Science Foundation and Information and Intelligent Systems (00-82016 ITR), the National

Institutes of Health and National Cancer Institute (CA87017), the University of Central Florida Presidential Instrumentation Initiative, and the Defense Advanced Research Projects Agency and the National Science Foundation Photonics Technology Access Program.

References

1. D. Huang, E. A. Swanson, C. P. Lin, J. S. Schuman, W. G. Stinson, W. Chang, M. R. Hee, T. Flotte, K. Gregory, C. A. Pulifito, and J. G. Fujimoto, "Optical coherence tomography," Science **254,** 1178–1181 (1991).
2. G. J. Tearney, B. E. Bouma, S. A. Boppart, B. Golubovic, E. A. Swanson, and J. G. Fujimoto, "Rapid acquisition of *in vivo* biological images by use of optical coherence tomography," Opt. Lett. **21,** 1408–1410 (1996).
3. A. M. Rollins, M. D. Kulkarni, S. Yazdanafar, R. Ungarunyawee, and J. A. Izatt, "*In vivo* video rate optical coherence tomography," Opt. Express **3,** 219–229 (1998), www.opticsexpress.org.
4. D. L. Marks, A. L. Oldenburg, J. J. Reynolds, and S. A. Boppart, "Digital algorithm for dispersion correction in optical coherence tomography for homogeneous and stratified media," Appl. Opt. **42,** 204–217 (2003).
5. A. F. Fercher, C. K. Hitzenberger, M. Sticker, and R. Zawadzki, "Numerical dispersion compensation for partial coherence interferometry and optical coherence tomography," Opt. Express **9,** 610–615 (2001), www.opticsexpress.org.
6. D. L. Marks, A. L. Oldenburg, J. J. Reynolds, and S. A. Boppart, "Autofocus algorithm for dispersion correction in optical coherence tomography," Appl. Opt. **42,** 3038–3046 (2003).
7. R. A. Leitgeb, W. Drexler, A. Unterhuber, B. Hermann, T. Bajraszewski, T. Le, A. Stingl, and A. F. Fercher, "Ultrahigh resolution Fourier domain optical coherence tomography," Opt. Express **12,** 2156–2165 (2004), www.opticsexpress.org.
8. M. Wojtkowski, V. J. Srinivasan, T. H. Ko, J. G. Fujimoto, A. Kowalczyk, and J. S. Duker, "Ultrahigh-resolution, high-speed, Fourier domain optical coherence tomography and methods for dispersion compensation," Opt. Express **12,** 2404–2422 (2004), www.opticsexpress.org.
9. B. Cense, N. A. Nassif, T. C. Chen, M. C. Pierce, S. Yun, B. H. Park, B. E. Bouma, G. J. Tearney, and J. F. de Boer, "Ultrahigh-resolution high-speed retinal imaging using spectral-domain optical coherence tomography," Opt. Express **12,** 2435–2447 (2004), www.opticsexpress.org.
10. E. D. J. Smith, A. V. Zvyagin, and D. D. Sampson, "Real-time dispersion compensation in scanning interferometry," Opt. Lett. **27,** 1998–2000 (2002).
11. K. F. Kwong, D. Yankelevich, K. C. Chu, J. P. Heritage, and A. Dienes, "400-Hz mechanical scanning optical delay line," Opt. Lett. **18,** 558–561 (1993).
12. G. J. Tearney, B. E. Bouma, and J. G. Fujimoto, "High-speed phase- and group-delay scanning with a grating-based phase control delay line," Opt. Lett. **22,** 1811–1812 (1997).
13. W. K. Niblack, J. O. Schenk, B. Liu, and M. E. Brezinski, "Dispersion in a grating-based optical delay line for optical coherence tomography," Appl. Opt. **42,** 4115–4118 (2003).
14. I. Hsu, C. Sun, C. Lu, C. C. Yang, C. Chiang, and C. Lin, "Resolution improvement with dispersion manipulation and a retrieval algorithm in optical coherence tomography," Appl. Opt. **42,** 227–234 (2003).
15. M. B. Nasr, B. E. A. Saleh, A. V. Sergienko, and M. Teich, "Dispersion-cancelled and dispersion-sensitive quantum optical coherence tomography," Opt. Express **12,** 1353–1362 (2004), www.opticsexpress.org.
16. Y. Wang, J. Stuart Nelson, Z. Chen, B. J. Reiser, R. S. Chuck, and R. S. Windeler, "Optimal wavelength for ultrahigh-resolution optical coherence tomography," Opt. Express **11,** 1411–1417 (2003), www.opticsexpress.org.
17. A. V. Zvyagin, E. D. J. Smith, and D. D. Sampson, "Delay and dispersion characteristics of a frequency-domain optical delay line for scanning interferometry," J. Opt. Soc. Am. A **20,** 333–341 (2003).
18. H. H. Barrett, K. J. Myers, and B. E. A. Saleh, eds., *Foundations of Image Science, Wiley Series in Pure and Applied Optics* (Wiley, Hoboken, N.J., 2004).
19. J. W. Goodman, *Statistical Optics* (Wiley, New York, 1985).
20. T. L. Troy and S. N. Thennadil, "Optical properties of human skin in the near infrared wavelength range of 1000 to 2200 nm," J. Biomed. Opt. **6,** 167–176 (2001).
21. K. S. Abedin and H. Ito, "Temperature-dependent dispersion relation of ferroelectric lithium tantalite," J. Appl. Phys. **80,** 6561–6563 (1996).
22. T. I. Lakoba and G. P. Agrawal, "Effects of third-order dispersion on dispersion-managed solitons," J. Opt. Soc. Am. B **16,** 1332–1343 (1999).
23. G. P. Agrawal, *Nonlinear Fiber Optics* (Academic, San Diego, Calif., 1995).
24. C. Akcay, P. Parrein, and J. P. Rolland, "Estimation of longitudinal resolution in optical coherence imaging," Appl. Opt. **41,** 5256–5262 (2002).
25. E. Sorokin, G. Tempea, and T. Brabec, "Measurement of the root-mean-square width and the root-mean-square chirp in ultrafast optics," J. Opt. Soc. Am. B **17,** 146–150 (2000).